

# Spatial Angular Pseudo-Derivative Searching: A Single Snapshot Super-resolution Sparse DOA Scheme with Potential for Practical Application

Longxin Bai, Jingchao Zhang, and Liyan Qiao

## I. INTRODUCTION

While super-resolution direction-of-arrival (DOA) estimation has been extensively studied for over four decades [1], [2], achieving real-time accuracy remains a formidable challenge under stringent constraints such as limited computational resources, restricted array apertures, and the single-snapshot constraint. Notably, this technology is pivotal for automotive millimeter-wave (mmWave) radars, where it enables critical perception tasks within autonomous driving systems and robotic environments [3], [4], [5], [6], [7]. Therefore, addressing these challenges to enhance the angular estimation performance of mmWave radars is essential to meet the requirements [8] of next-generation autonomous driving.

In autonomous driving scenarios, the DOA estimation process must be executed for all Range-Doppler (RD) cells [9] identified by Constant False Alarm Rate (CFAR) detection within the strict duration of a single frame interval. Typically, the frame interval of automotive mmWave radars is less than 50 ms, during which multiple RD cells must be processed [10], [11]. Considering the time overhead incurred by post-processing following point cloud generation, computational efficiency becomes the primary prerequisite for the practicality of any super-resolution DOA algorithm. Failure to achieve effective DOA estimation within the required time frame inevitably results in the loss of critical target information, thereby compromising the integrity of the generated point clouds and severely undermining the reliability of the downstream radar processing pipeline. In addition, estimation accuracy and angular resolution are equally vital metrics for evaluating super-resolution DOA algorithms. Consequently, a super-resolution DOA algorithm with practical potential needs to simultaneously provide low computational complexity, high accuracy, and superior angular resolution [8].

This work has been submitted to the IEEE for possible publication. Copyright may be transferred without notice, after which this version may no longer be accessible.

This work is supported by National Natural Science Foundation of China under Grant 61701138, the Natural Science Foundation of Heilongjiang Province of China under Grant LH2022F019, Hei Long Jiang Postdoctoral Foundation under Grant LBH-Z16087 and the Fundamental Research Funds for the Central Universities under Grant HIT.NSRIF202339. (Corresponding author: Jingchao Zhang)

L. Bai, J. Zhang, and L. Qiao are with School of Electronics and Information Engineering, Harbin Institute of Technology, Harbin 150001, China.(e-mail: bailongxin@stu.hit.edu.cn, zhangjingchao@hit.edu.cn, qiaoliyan@hit.edu.cn)

## A. Prior work

Taking radar simultaneous localization and mapping (SLAM) as a representative post-processing scenario, DOA estimation typically relies on spatial Discrete Fourier Transforms (DFT) or conventional beamforming (CBF) techniques, such as Bartlett beamforming, to satisfy real-time constraints [6], [7], [12]. CBF is capable of performing DOA estimation with only a single snapshot and exhibits inherent robustness to coherent signals. However, the angular resolution of these methods is fundamentally constrained by the array aperture, a physical boundary known as the Rayleigh limit [13]. In many DOA estimation studies [1], [2], [14], [15], [16], when the angular separation of two sources falls within the Rayleigh limit, the CBF spatial spectrum is generally considered to fail to resolve the sources due to peak merging. Consequently, the information embedded within such spectra is rarely further exploited. Recently, Itzhak et al. [17] proposed a maximum array gain beamforming method designed to minimize signal distortion across a predefined region of interest (ROI). While this approach more effectively leverages information within the spatial spectrum by accounting for all directions within the ROI, it is primarily intended for signal enhancement and does not provide explicit DOA estimates. In addition to limited angular resolution, the estimation accuracy of CBF is inferior to that of super-resolution algorithms. This lack of precision exacerbates the accumulation of errors within the SLAM framework, thereby complicating downstream processing tasks [7], [18].

To surpass the Rayleigh limit, various super-resolution DOA estimation algorithms have been developed, most notably subspace-based methods such as MUSIC [19] and ESPRIT [20]. However, these algorithms typically require the accumulation of multiple snapshots to accurately estimate the signal covariance matrix. In dynamic scenarios involving moving radar platforms or maneuvering targets, this requirement is often untenable, as the non-stationarity of the signal leads to significant estimation bias in the sample covariance matrix. Consequently, subspace-based methods have limited applicability in high-mobility radar environments [8].

Alternatively, maximum likelihood (ML) estimation methods [1] can achieve high-precision super-resolution in single-snapshot scenarios. However, their prohibitive

computational complexity generally precludes real-time implementation on embedded platforms. Although recent work by Wu et al. [11] leveraged the massive parallelism of NVIDIA V100 GPUs to optimize deterministic ML (DML) [1] for real-time operation, this approach does not address the fundamental algorithmic complexity; instead, it relies on high-performance hardware, which increases system cost and power consumption. Such hardware-intensive solutions are beyond the scope of this study. By the same token, deep learning-based DOA estimation methods that necessitate high-performance GPUs for training or inference are also considered beyond the scope of this study.

Setting aside computational complexity, sparse signal recovery based algorithms represent another class of DOA estimation methods suitable for mobile platforms. The fundamental principle involves transforming the array manifold into an over-complete dictionary based on a predefined spatial grid. In the noiseless case, the resulting spatial signal vector is inherently sparse, where all entries are zero except those corresponding to the true directions of arrival [21]. While this objective is ideally formulated as an  $\ell_0$ -norm minimization, it is well known to be a classic NP-hard problem [18]. Consequently, various strategies [14] have been proposed to address the challenges associated with  $\ell_0$ -norm minimization.

The first category encompasses penalty-based relaxation methods, which employ surrogate functions to approximate the  $\ell_0$ -norm, thereby rendering the optimization problem computationally tractable in polynomial time. For instance, Malioutov et al. [21] introduced the  $\ell_1$ -SVD algorithm by replacing the  $\ell_0$ -norm with an  $\ell_1$ -norm relaxation. This framework was subsequently extended to include weighted  $\ell_1$ -norm minimization strategies in [22], [23]. Furthermore, non-convex penalties, such as the continuous exact  $\ell_0$  (CEL0) [24], [25] and the trimmed Lasso [26], have also been extensively investigated in the literature. A second category comprises greedy algorithms, most notably orthogonal matching pursuit (OMP) [27], which iteratively select atoms to reconstruct the signal with low computational overhead. Nevertheless, in our simulations, we observed that OMP fails to provide the necessary precision for high-resolution DOA estimation.

Sparse recovery can also be addressed within a probabilistic framework. By adopting a Bayesian perspective, one can reformulate DOA estimation as a posterior inference problem. Specifically, sparse Bayesian learning (SBL) models signal sparsity through a hierarchical Gaussian prior [28], [29], enabling efficient hyperparameter estimation via the expectation maximization (EM) algorithm. Alternatively, a Laplace prior [30], [31] may be employed to more directly promote sparsity, mirroring the characteristics of the  $\ell_1$ -norm. Although the resulting posterior is often analytically intractable, variational inference (VI) [32] provides a robust means of approximation. To circumvent the limitations of discretization entirely, gridless estimation approaches [33], [34] have been introduced. These methods operate in a continuous parameter space,

effectively eliminating the off-grid issue by leveraging theories such as atomic norm minimization.

A major bottleneck of these high-accuracy sparse recovery methods is their prohibitive computational complexity, primarily stemming from the intensive iterative procedures required for convergence. Irrespective of whether grid evolution schemes are employed [35], [36], the underlying optimization tasks remain computationally demanding. In the context of automotive radar, such overhead often impedes real-time implementation. While various acceleration strategies have been explored [37], [38], they typically result in a pronounced degradation of super-resolution performance.

## B. Contribution

To bridge the gap between sparse signal recovery theory and practical implementation, this paper proposes a sparse DOA estimation scheme tailored to meet the real-time, high-accuracy, and high-resolution requirements of automotive radar systems. The crux of the proposed method lies in the discovery that the off-grid model, in conjunction with the spatial grid, exhibits a property analogous to a first-order derivative relative to the true DOAs. This characteristic is termed the spatial angular pseudo-derivative. By leveraging this property, we reformulate the sparse DOA estimation problem, transforming it from a computationally intensive high-dimensional optimization into an efficient grid search procedure. We define and characterize the spatial angular pseudo-derivative, a mathematical property that endows discrete grid points with directional information relative to the true targets. The main contributions of this work are summarized as follows:

- By integrating this property as a constraint into the standard  $\ell_0$ -norm minimization framework, we propose a novel optimization objective. This formulation provides a more faithful representation of the physical characteristics inherent in DOA estimation compared to the conventional  $\ell_0$ -norm. Meanwhile, the proposed modeling paradigm naturally translates the problem into an efficient grid-search-based solution scheme.
- We propose the computationally efficient SAPD search algorithm. By leveraging the properties of the spatial angular pseudo-derivative, this algorithm circumvents large-scale matrix inversions and intensive iterative procedures. The process begins with initialization using the spatial spectrum obtained via Bartlett beamforming, followed by a targeted search for the ground-truth DOAs. A greedy patch mechanism is integrated to address complex scenarios and recover potential missed detections in the initial support set, thereby ensuring real-time, high-precision, and high-resolution DOA estimation for automotive radar systems.
- An analysis of the computational complexity and convergence properties of the SAPD algorithm is provided.

- Numerical simulations and experimental validation demonstrate that the proposed method achieves superior performance in terms of real-time operation, high precision, and high resolution for automotive radar DOA estimation.

The rest of this paper is organized as follows. Section II details the signal model and provides a preliminary analysis of the sparse DOA estimation framework. Section III introduces the proposed optimization objective based on the spatial angular pseudo-derivative, followed by the associated solver and its corresponding complexity and convergence analysis. Section IV presents the numerical simulations. Section V provides concluding remarks.

Notations:  $\|\cdot\|_2$ ,  $\|\cdot\|_1$  denote the  $\ell_2$ -norm and  $\ell_1$ -norm, respectively.  $(\cdot)^T$ ,  $(\cdot)^H$ ,  $(\cdot)^{-1}$  and  $(\cdot)^\dagger$  represent the transposition, Hermitian transposition, inversion, pseudo-inversion, respectively.  $\lceil \cdot \rceil$  and  $\text{round}(\cdot)$  denote the ceiling and rounding operators, respectively.  $\mathbb{E}(\cdot)$  denotes the expectation operator.  $j = \sqrt{1}$ .  $\mathbf{1}_N$  is the  $N \times 1$  all-ones vector.  $[n] = \{1, \dots, n\}$ .  $\text{sgn}(\cdot)$  denotes the signum function.

## II. Problem Statement and Preliminary Analysis

Consider a frequency-modulated continuous waveform (FMCW) radar system equipped with a uniform linear array (ULA) of  $M$  receive antennas. The array receives echoes from  $K$  far-field sources impinging from direction  $\boldsymbol{\theta}^* = [\theta_1^*, \theta_2^*, \dots, \theta_K^*]$ . We assume that these  $K$  sources are located within the same RD cell. The spacing between adjacent antennas is  $d_r = \lambda_r/2$ , where  $\lambda_r$  is the wavelength of the echo signal. Under far-field and narrowband assumptions, the time delays of signals arriving at different antennas are represented as phase shifts. For the  $k$ -th source, where  $k = 1, \dots, K$ , these phase shifts across the  $M$  antennas form the steering vector, which is formulated as

$$\mathbf{a}(\theta_k^*) = [1, e^{-j\pi \sin(\theta_k^*)}, \dots, e^{-j\pi(N-1) \sin(\theta_k^*)}]^T. \quad (1)$$

The received signal at the  $l$ -th snapshot is the superposition of the echoes from the  $K$  targets. Under ideal conditions, the observation vector is given by

$$\mathbf{y}(l) = \sum_{k=1}^K \mathbf{a}(\theta_k^*) \mathbf{s}(l) + \mathbf{n}(l) = \mathbf{A}(\boldsymbol{\theta}^*) \mathbf{s}(l) + \mathbf{n}(l), \quad (2)$$

where  $\mathbf{A}(\boldsymbol{\theta}^*) = [\mathbf{a}(\theta_1^*), \mathbf{a}(\theta_2^*), \dots, \mathbf{a}(\theta_K^*)] \in \mathbb{C}^{M \times K}$  is the array manifold matrix,  $\mathbf{s}(l) \in \mathbb{C}^K$  denotes the signal vector, and  $\mathbf{n}(l) \in \mathbb{C}^M$  represents the additive white Gaussian noise (AWGN) vector. For notational simplicity, we suppress the index  $l$ , reintroducing it only when essential for clarity.

In conventional radar signal processing, the angular domain is discretized into a uniform spatial grid  $\boldsymbol{\theta} = [\theta_1, \theta_2, \dots, \theta_G]^T$  with a grid interval of  $\Delta\theta$ . We employ Bartlett beamforming to estimate the power at each spatial grid point, denoted by  $P_g(\theta)$  for  $\theta \in \boldsymbol{\theta}$ . In the spatial spectrum, the power at each grid point is determined by the quadratic form of the steering vector

and the covariance matrix of the received signal, expressed as

$$P_g(\theta) = \mathbf{a}^H(\theta) \mathbf{R}_y \mathbf{a}(\theta) = \mathbf{a}^H(\theta) \mathbb{E}[\mathbf{y} \mathbf{y}^H] \mathbf{a}(\theta), \quad (3)$$

where  $\mathbf{R}_y$  denotes the observation data covariance matrix. In the single-snapshot case, this expression simplifies to  $P_g(\theta) = |\mathbf{a}^H(\theta) \mathbf{y}|^2$ . We define the vectorized spatial spectrum as  $P_g(\boldsymbol{\theta}) \in \mathbb{R}^G$ , where each element corresponds to the power estimated at the respective grid point. The spatial spectrum encapsulates significant information regarding the spatial distribution of the targets, providing the basis for the initialization of our proposed scheme.

To provide physical intuition, this section presents a characterization of the spatial spectrum. Let  $n_f$  and  $P_{s_1}$  denote the noise floor and the reference power level of a single-source power within a single beam, respectively. Specifically, the angular separation between the two half-power points of a spectral peak is defined as the half-power beamwidth, also referred to as the 3-dB beamwidth  $\theta_{3\text{dB}}$ , which characterizes the Rayleigh resolution limit. The set of spectral peaks  $\mathcal{P}$ , corresponding to potential incident angles, is formulated as

$$\mathcal{P} = \{p_i \mid p_i = P_g(\bar{\theta}_i) > p_t, \bar{\theta}_i \in \boldsymbol{\theta}, i = [D]\}, \quad (4)$$

where  $p_t$  denotes the peak detection threshold satisfying  $n_f < p_t < P_{s_1}$ . Due to the constraints of the Rayleigh resolution limit, the number of resolved peaks  $D$  satisfies  $D \leq K$ . Given the precision constraints of Bartlett beamforming, the true DOAs are assumed to reside in the vicinity of the observed peaks. In a representative scenario where  $K = 2$  sources result in a single merged peak ( $D = 1$ ), a beamwidth  $L_{\mathcal{B}_i}$  exceeding  $\theta_{3\text{dB}}$  signifies that multiple targets are unresolved within the same beam. In such cases, the true incident angles are distributed on either side of the estimated peak position  $\bar{\theta}_i$  [13].

Within the sparse signal representation framework, the overcomplete array manifold matrix  $\mathbf{A}(\boldsymbol{\theta}) = [\mathbf{a}(\theta_1), \mathbf{a}(\theta_2), \dots, \mathbf{a}(\theta_G)]$  is formulated using the discretized spatial grid  $\boldsymbol{\theta}$ . Consequently, the observation model for DOA estimation is expressed as  $\mathbf{y} = \mathbf{A}(\boldsymbol{\theta}) \mathbf{x} + \mathbf{n}$ , where  $\mathbf{x} \in \mathbb{C}^G$  is a sparse signal vector. Let  $\mathbf{I}$  denote the support set corresponding to the non-zero entries of  $\mathbf{x}$ , where  $\|\mathbf{x}\|_0 = |\mathbf{I}| = K$ . The objective of sparse signal recovery is formulated as the following  $\ell_0$ -norm minimization problem

$$\hat{\mathbf{x}} = \arg \min_{\mathbf{x}} \|\mathbf{x}\|_0 \quad \text{s.t.} \quad \mathbf{y} = \mathbf{A}(\boldsymbol{\theta}) \mathbf{x}. \quad (5)$$

(5) is a combinatorial optimization problem that can be addressed via an exhaustive search method [18]. For an index set  $\mathcal{G} = \{g_1, g_2, \dots, g_d\} \subset [G]$  with cardinality  $|\mathcal{G}| = d \leq K$ , we define the corresponding angular vector  $\boldsymbol{\theta}_{\mathcal{G}} \subset \boldsymbol{\theta}$  and the vector  $\mathbf{x}_{\mathcal{G}} \subset \mathbf{x}$  as

$$\boldsymbol{\theta}_{\mathcal{G}} = [\theta_{g_1}, \theta_{g_2}, \dots, \theta_{g_d}], g_i \in \mathcal{G}, \quad (6)$$

$$\mathbf{x}_{\mathcal{G}} = [x_{g_1}, x_{g_2}, \dots, x_{g_d}]^T, g_i \in \mathcal{G}. \quad (7)$$

Furthermore, let  $\Lambda_s = \{\mathcal{G}_i \mid \mathcal{G}_i \subset [G], 1 \leq |\mathcal{G}_i| \leq K\}$  denote the collection of all candidate support sets. For a given

candidate support  $\mathcal{G}_i$ , the signal vector  $\mathbf{x}_{\mathcal{G}_i}$  is obtained via the least-squares (LS) criterion, expressed as

$$\mathbf{x}_{\mathcal{G}_i} = \mathbf{x}(\boldsymbol{\theta}_{\mathcal{G}_i}) = (\mathbf{A}(\boldsymbol{\theta}_{\mathcal{G}_i})^H \mathbf{A}(\boldsymbol{\theta}_{\mathcal{G}_i}))^{-1} \mathbf{A}(\boldsymbol{\theta}_{\mathcal{G}_i})^H \mathbf{y}. \quad (8)$$

Equation (8) explicitly formulates  $\mathbf{x}_{\mathcal{G}_i}$  as a function of the angular vector  $\boldsymbol{\theta}_{\mathcal{G}_i}$ . If  $\mathbf{x}_{\mathcal{G}_i}$  satisfies the measurement consistency condition  $\mathbf{y} = \mathbf{A}(\boldsymbol{\theta}_{\mathcal{G}_i})\mathbf{x}_{\mathcal{G}_i}$ , then the reconstructed solution  $\hat{\mathbf{x}}$  is defined on the support  $\mathbf{I} = \mathcal{G}_i$  such that  $\hat{\mathbf{x}}_{\mathbf{I}} = \mathbf{x}_{\mathcal{G}_i}$  and  $\hat{\mathbf{x}}_{\mathbf{I}^c} = 0$ . While the proposed approach does not utilize the exhaustive search method to solve (5), this paradigm underscores the explicit functional dependence of  $\mathbf{x}_{\mathcal{G}_i}$  on the corresponding angular set  $\boldsymbol{\theta}_{\mathcal{G}_i}$  within the discretized spatial grid.

In practice, target DOAs seldom coincide with the discrete grid points  $\boldsymbol{\theta}$ . Accordingly, the  $k$ -th incident angle  $\theta_k^*$  can be reformulated as

$$\theta_k^* = \theta_g + (\theta_k^* - \theta_g) = \theta_g + \beta_k, \quad \theta_g \in \boldsymbol{\theta}. \quad (9)$$

We refer to (9) as the bias model. This terminology is adopted to provide a more generalized framework than the conventional off-grid model, facilitating the exposition of the methodology developed in the subsequent sections. Let  $\theta_{g_k}$  denote the grid point nearest to  $\theta_k^*$ . By employing a first-order Taylor expansion [28], the steering vector  $\mathbf{a}(\theta_k^*)$  is expressed as

$$\mathbf{a}(\theta_k^*) = \mathbf{a}(\theta_{g_k} + \beta_k) \approx \mathbf{a}(\theta_{g_k}) + \mathbf{b}(\theta_{g_k})\beta_k, \quad (10)$$

where  $\mathbf{b}(\theta_{g_k}) = \mathbf{a}'(\theta_{g_k})$  represents the steering vector derivative evaluated at the grid point  $\theta_{g_k}$ . Substituting the linearized approximation into the array signal model, the off-grid observation model is formulated as

$$\mathbf{y} = \mathbf{A}(\boldsymbol{\theta})\mathbf{x} + \mathbf{B}(\boldsymbol{\theta})\text{diag}(\boldsymbol{\beta})\mathbf{x}, \quad (11)$$

where  $\mathbf{B} = [\mathbf{b}(\theta_1), \mathbf{b}(\theta_2), \dots, \mathbf{b}(\theta_G)]$  is the matrix of steering vector derivatives and  $\boldsymbol{\beta} = [\beta_1, \beta_2, \dots, \beta_G]^T \in \mathbb{R}^G$  denotes the vector of off-grid offsets.

Once  $\boldsymbol{\theta}_{\mathcal{G}} = [\theta_{g_1}, \theta_{g_2}, \dots, \theta_{g_K}]^T$  and  $\mathbf{x}(\boldsymbol{\theta}_{\mathcal{G}})$  have been determined, the off-grid bias vector  $\boldsymbol{\beta}$  can be estimated. By utilizing the identity  $\text{diag}(\boldsymbol{\beta}_{\mathcal{G}})\mathbf{x}_{\mathcal{G}} = \text{diag}(\mathbf{x}_{\mathcal{G}})\boldsymbol{\beta}_{\mathcal{G}}$ , the observation model is rewritten as  $\mathbf{y} = \mathbf{A}(\boldsymbol{\theta}_{\mathcal{G}})\mathbf{x}_{\mathcal{G}} + \mathbf{B}(\boldsymbol{\theta}_{\mathcal{G}})\text{diag}(\mathbf{x}_{\mathcal{G}})\boldsymbol{\beta}_{\mathcal{G}}$ . Therefore, the estimation of  $\boldsymbol{\beta}_{\mathcal{G}}$  can be modeled as the following constrained least-squares problem

$$\boldsymbol{\beta}_{\mathcal{G}} = \arg \min_{\boldsymbol{\beta}_{\mathcal{G}} \in \mathbb{R}^K} \|\tilde{\mathbf{y}} - \tilde{\mathbf{B}}(\boldsymbol{\theta}_{\mathcal{G}})\boldsymbol{\beta}_{\mathcal{G}}\|_2^2, \quad (12)$$

where  $\tilde{\mathbf{y}} = \mathbf{y} - \mathbf{A}(\boldsymbol{\theta}_{\mathcal{G}})\mathbf{x}_{\mathcal{G}}$  and  $\tilde{\mathbf{B}}(\boldsymbol{\theta}_{\mathcal{G}}) = \mathbf{B}(\boldsymbol{\theta}_{\mathcal{G}})\text{diag}(\mathbf{x}_{\mathcal{G}})$ . Under the real-valued constraint  $\boldsymbol{\beta}_{\mathcal{G}} \in \mathbb{R}^{|\mathcal{G}|}$ , the closed-form solution to (12) is given by

$$\boldsymbol{\beta}_{\mathcal{G}} = \boldsymbol{\beta}(\boldsymbol{\theta}_{\mathcal{G}}) = \{\text{Re}(\tilde{\mathbf{B}}(\boldsymbol{\theta}_{\mathcal{G}})^H \tilde{\mathbf{B}}(\boldsymbol{\theta}_{\mathcal{G}}))\}^{-1} \cdot \text{Re}\{\tilde{\mathbf{B}}(\boldsymbol{\theta}_{\mathcal{G}})^H \tilde{\mathbf{y}}\}. \quad (13)$$

As indicated by (13), the estimated bias  $\boldsymbol{\theta}_{\mathcal{G}}$  can be viewed as an explicit function of the grid points  $\boldsymbol{\theta}_{\mathcal{G}}$ . We refer to the expression in (13) as the spatial angular pseudo-derivative, the properties of which are elaborated in the subsequent section.

The spatial spectrum obtained via Bartlett Beamforming encapsulates rich information regarding the source

distribution, which can be leveraged as prior knowledge for sparse DOA estimation. However,  $\ell_0$ -norm minimization is a general sparse recovery framework not specifically tailored to the unique geometry of the DOA problem. In light of this preliminary analysis, we argue that the conventional formulation in (5) provides an insufficient characterization, as it neglects critical physical insights. To address this, the present work formulates a novel optimization objective incorporating the spatial angular pseudo-derivative, which more accurately characterizes the physical properties of the DOA estimation problem, and develops an associated computationally efficient solver.

### III. Spatial Angular Pseudo-Derivative Search Algorithm

This section presents the novel optimization objective function developed for the DOA estimation problem and describes its associated solver, the spatial angular pseudo-derivative search algorithm. Our key insight is that the grid bias  $\boldsymbol{\beta}_{\mathcal{G}}$  formulated in (12) endows the spatial grid points  $\boldsymbol{\theta}_{\mathcal{G}}$  with a property analogous to a first-order derivative. We term this property the spatial angular pseudo-derivative. This property not only ensures that the proposed cost function more faithfully captures the underlying structure of the DOA estimation problem compared to  $\ell_0$ -norm minimization, but also gives rise to the spatial angular pseudo-derivative search algorithm, which simultaneously achieves super-resolution performance, low computational complexity, and high estimation accuracy.

#### A. Proposed Objective and spatial angular pseudo-derivative concept

Based on the definition of the bias model (9), the true incident angles are characterized by the conditions

$$\boldsymbol{\beta}(\boldsymbol{\theta}^* - \Delta\boldsymbol{\theta}) > \mathbf{0}, \quad \boldsymbol{\beta}(\boldsymbol{\theta}^* + \Delta\boldsymbol{\theta}) < \mathbf{0}, \quad (14)$$

where  $\Delta\boldsymbol{\theta} = \Delta\theta \cdot \mathbf{1}_K$ . A schematic illustration of this property is shown in Fig.1. The aforementioned conditions constitute essential criteria for a valid estimation estimate. Consequently, we augment the original  $\ell_0$ -norm minimization problem with these new constraints to formulate the proposed optimization problem

$$(P_D) \quad \begin{aligned} & \arg \min_{\boldsymbol{\theta}_{\mathcal{G}}} \|\mathbf{y} - \mathbf{A}(\boldsymbol{\theta}_{\mathcal{G}})\mathbf{x}(\boldsymbol{\theta}_{\mathcal{G}})\|_2 \\ & \text{s.t. } |\mathcal{G}| = K, \quad \boldsymbol{\beta}(\boldsymbol{\theta}_{\mathcal{G}} - \Delta\boldsymbol{\theta}) > \mathbf{0}, \quad \boldsymbol{\beta}(\boldsymbol{\theta}_{\mathcal{G}} + \Delta\boldsymbol{\theta}) < \mathbf{0}. \end{aligned} \quad (15)$$

To facilitate the subsequent discussion and derivation, we define the following two functions to simplify the optimization problem

$$\boldsymbol{\varepsilon}(\boldsymbol{\theta}_{\mathcal{G}}) = \|\mathbf{y} - \mathbf{A}(\boldsymbol{\theta}_{\mathcal{G}})\mathbf{x}(\boldsymbol{\theta}_{\mathcal{G}})\|_2 \quad (16)$$

$$h(\boldsymbol{\theta}_{\mathcal{G}}) = \text{sgn}(\boldsymbol{\beta}(\boldsymbol{\theta}_{\mathcal{G}} - \Delta\boldsymbol{\theta})) + \text{sgn}(\boldsymbol{\beta}(\boldsymbol{\theta}_{\mathcal{G}} + \Delta\boldsymbol{\theta})). \quad (17)$$

Accordingly, the optimization problem can be compactly reformulated as

$$\begin{aligned} & \min_{\boldsymbol{\theta}_{\mathcal{G}}} \quad \boldsymbol{\varepsilon}(\boldsymbol{\theta}_{\mathcal{G}}) \\ & \text{s.t. } |\mathcal{G}| = K, \quad h(\boldsymbol{\theta}_{\mathcal{G}}) = \mathbf{0}. \end{aligned} \quad (18)$$

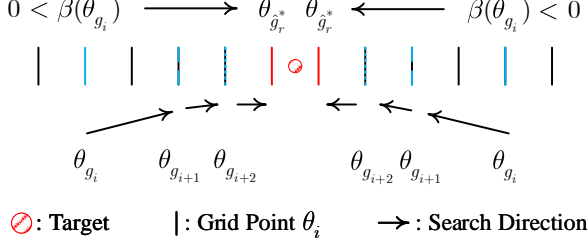


Fig. 1: Spatial angular pseudo-derivative schematic diagram

Prior to detailing the solution to the optimization problem, we further elucidate the implications of the spatial angular pseudo-derivative  $\beta(\theta_{\mathcal{G}})$ . For the sake of clarity, we make the following assumptions.  $|\mathcal{G}| = K$ . Without loss of generality, the incident angles are ordered such that  $\theta_1^* < \theta_2^* < \dots < \theta_K^*$ . Following the ordering of the true angles, the elements in  $\theta_{\mathcal{G}}$  are indexed in ascending order, such that  $\theta_{g_1} < \theta_{g_2} < \dots < \theta_{g_K}$ . For any  $\theta_k^* \in \theta^*$ , we introduce the function defined by

$$d(\theta_{\mathcal{G}}, \theta_k^*) = \{d_i | d_i = |\theta_k^* - \theta_{g_i}|, \theta_{g_i} \in \theta_{\mathcal{G}}, i \in [K]\}. \quad (19)$$

$\theta_{\mathcal{G}}$  is required to satisfy the condition

$$k = \arg \min_{i \in [K]} d(\theta_{\mathcal{G}}, \theta_k^*). \quad (20)$$

This condition implies that  $\theta_{g_k}$  is the element in the set  $\theta_{\mathcal{G}}$  closest to the  $\theta_k^*$ .

Substituting  $\theta_{\mathcal{G}}$  into equation (8), (12), (16) yields  $\varepsilon(\theta_{\mathcal{G}})$  and  $\beta(\theta_{\mathcal{G}})$ . Under the aforementioned assumptions, it is highly probable that  $\varepsilon(\theta_{\mathcal{G}}) > \epsilon$ , which signifies a recovery failure. The parameter  $\epsilon$  governs the accuracy of the signal recovery. Consequently,  $\beta(\theta_{\mathcal{G}})$  can not be equated with the grid bias. However,  $\beta(\theta_{g_k})$  serves as a coarse metric of the spatial proximity to the target angle  $\theta_k$ . The magnitude of  $|\beta(\theta_{g_i})|$  is positively correlated with the angular deviation from the ground-truth  $\theta_k$ . Furthermore, by definition (12), it holds that  $\beta(\theta_{g_i}) > 0$ ,  $\theta_{g_i} < \theta_k$  and  $\beta(\theta_{g_i}) < 0$ ,  $\theta_{g_i} > \theta_k$ . Therefore, we observe that  $\beta(\theta_{g_i})$  manifests a unique rate of change at the current grid point  $\theta_{g_k}$  with respect to  $\theta_k$  within the spatial grid domain. We term  $\beta(\theta_{g_i})$  the spatial angular pseudo-derivative.

Substituting the grid points in the vicinity of  $\theta_{g_k}$  into (12) yields the corresponding values. According to the properties of spatial angular pseudo-derivative, the sequence of the magnitude of  $\beta(\theta_{g_i})$  manifest a convex distribution. By leveraging the discrete structure of the spatial grid, the target values can be determined via a grid-based search over the values of the spatial angular pseudo-derivative. This intuition serves as the underlying principle of the algorithm proposed in the subsequent subsection. This also represents a fundamental departure from traditional sparse reconstruction frameworks that are often hindered by high-complexity iterative steps. Thus, the optimization problem ( $P_D$ ) provides a more accurate

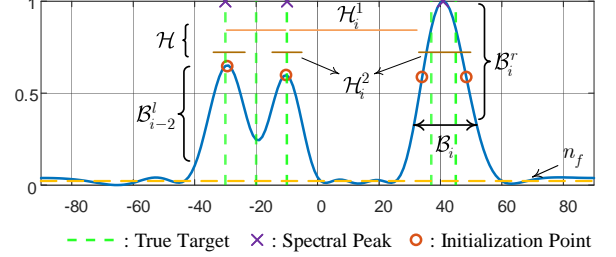


Fig. 2: Beam Feature Diagram

characterization of the DOA estimation problem than the standard  $\ell_0$ -norm formulation in (5).

### B. SAPD Scheme

This subsection details our proposed SAPD algorithm, which integrates an initialization procedure leveraging the CBF-based spatial spectrum, the SAPD search step, and a greedy patch mechanism designed to mitigate missed detections.

**Initialization Step:** First, a preliminary procedure such as Constant False Alarm Rate (CFAR) detection is applied to the spatial spectrum to estimate the noise floor  $n_f$ , identify the set of spectral peaks  $\mathcal{P}$ , and extract their respective beam regions  $\mathcal{B}_i$ .

To estimate the noise floor  $n_f$ , we identify the subset of grid points in the spatial spectrum that exhibit low power levels, which formulated as

$$\mathcal{N} = \{P_g(\theta_{m_i}) \mid \|P_g(\theta)\|_{\infty} - P_g(\theta_{m_i}) > \eta, m_i \in \mathcal{M}, \mathcal{M} \subset [G]\} \quad (21)$$

where  $\eta$  denotes a threshold employed to distinguish the background noise floor from the elevated local minima situated between adjacent spectral peaks. Then, the noise floor  $n_f$  is defined as the mean power of the grid points within the set  $\mathcal{N}$ .

Based on the set of spectral peaks  $\mathcal{P}$ , we define the following two sets

$$R_i^l = [\bar{\theta}_{i-1}, \bar{\theta}_i], R_i^r = [\bar{\theta}_i, \bar{\theta}_{i+1}]. \quad (22)$$

The two sets  $P_g(\theta_{R_i^l})$  and  $P_g(\theta_{R_i^r})$  are searched to identify the half-power points  $\theta_h^{l_i}$  and  $\theta_h^{r_i}$ . If the half-power points are not identified within either set, the local minimum between adjacent peaks is adopted as the effective half-power point. Thus, the beam region is given by

$$\mathcal{B}_i^l = [\theta_h^{l_i}, \bar{\theta}_i], \mathcal{B}_i^r = [\bar{\theta}_i, \theta_h^{r_i}], \mathcal{B}_i = \mathcal{B}_i^l \cup \mathcal{B}_i^r. \quad (23)$$

By the three defined intervals (23), we define the  $i$ -th beam feature as

$$L_l = \bar{\theta}_i - \theta_h^{l_i}, L_r = \bar{\theta}_i - \theta_h^{r_i}, L_{\mathcal{B}_i} = \theta_h^{r_i} - \theta_h^{l_i}. \quad (24)$$

During the initialization procedure, we posit that if  $L_{\mathcal{B}_i} > \theta_{3dB} + 2\Delta\theta$ , then the beam contains two incident angles. Otherwise, the beam contains one source.

Following the bisection principle, we initialize the angle as

$$\mathcal{I}_i = \mathcal{I}(\mathcal{B}_i) = \begin{cases} \{\bar{\theta}_i\}, & L_{\mathcal{B}_i} < \theta_{3dB} + 2\Delta\theta \\ \{\theta_{\mathcal{I}_i}^1, \theta_{\mathcal{I}_i}^2\}, & L_{\mathcal{B}_i} > \theta_{3dB} + 2\Delta\theta \end{cases}, \quad (25)$$

where

$$\theta_{\mathcal{I}_i}^1 = \lceil \frac{\bar{\theta}_i - \theta_h^{\mathcal{B}_i}}{2} \rceil, \quad \theta_{\mathcal{I}_i}^2 = \lceil \frac{\theta_h^{\mathcal{B}_i} - \bar{\theta}_i}{2} \rceil. \quad (26)$$

The angular initialization set can be formulated as

$$\mathcal{I} = \bigcup_{i=1}^{|\mathcal{P}|} \mathcal{I}_i. \quad (27)$$

We denote the corresponding index set as  $\mathcal{G}^{(0)}$ . A schematic illustration of the results is shown in Fig.2. The steps of the initialization process are outlined in Algorithm 1.

---

#### Algorithm 1 Initialization via Spatial Spectrum

---

Input: The observation data  $\mathbf{y} \in \mathbb{C}^M$

Output: Initialization set  $\mathcal{G}^{(0)}$

- 1: Get the spatial spectrum  $P_g(\boldsymbol{\theta})$  via (3)
- 2: Get the noise floor  $n_f$ , the valid peaks set  $\mathcal{P}$  and the corresponding beam regions  $\mathcal{B} = \bigcup_{i=1}^{|\mathcal{P}|} = \mathcal{B}_i$
- 3: Analyze the features of each beam via (23) and (24)
- 4: for  $i = 1$  to  $|\mathcal{P}|$  do
- 5:     Get the initialization  $i$ -th beam via the (25).
- 6: end for
- 7: return The initialization set  $\mathcal{G}^{(0)}$  by (27).

---

**SAPD Search Step:** Based on (8) and (12), the SAPD search step can be viewed as depending exclusively on the given grid index set  $\mathcal{G}$ . Furthermore, the objective function (18) reveals that the optimization primarily hinges on the sign and magnitude of  $\boldsymbol{\beta}(\theta_{g_i})$ . Consequently, the true DOAs can be identified by performing successive updates on the index set  $\mathcal{G}$ . We denote the index set at the  $t$ -th iteration as  $\mathcal{G}^{(t)}$ .

1) Search step size: For notational convenience, we denote  $\boldsymbol{\beta}(\theta_{\mathcal{G}^{(t)}})$  as  $\boldsymbol{\beta}_t$ . The parameters  $\mathcal{V}_t$  governing the  $t$ -th search step size are defined as

$$\mathcal{V}_t = \begin{cases} N_1 \text{ round}(\boldsymbol{\beta}_{t-1}), & \boldsymbol{\beta}_{t-1} > \Delta\theta \\ N_2, & \Delta\theta/2 < \boldsymbol{\beta}_{t-1} < \Delta\theta, \\ 1, & \boldsymbol{\beta}_{t-1} < \Delta\theta/2 \end{cases}, \quad (28)$$

where  $N_1, N_2 \in \mathbb{Z}_+$ . Then, the search step size is defined as

$$\mathcal{S}_t = \mathcal{V}_t \cdot \text{sgn}(\boldsymbol{\beta}_{t-1}) \quad (29)$$

The updating grid index  $\mathcal{G}^{(t)}$  is given by

$$\mathcal{G}^{(t)} = \mathcal{G}^{(t-1)} + \mathcal{S}_t. \quad (30)$$

The spatial grid interval  $\Delta\theta$  is recommended to be set to  $1^\circ$ . Adopting a finer grid resolution is discouraged, as it significantly increases the number of search iterations and the computational overhead. Accordingly, the values of  $N_1$  and  $N_2$  are suggested to be 2.

2) Termination criterion: The function  $\mathcal{C}(t)$  for the convergence is given by

$$\mathcal{C}(t) = \mathcal{S}_{t-2} + \mathcal{S}_{t-1} + \mathcal{S}_t. \quad (31)$$

Under the condition  $\mathcal{C}(t) = 3 * |\mathcal{G}^{(0)}|$ , the search process ceases if  $\mathcal{G}^{(t-2)} = \mathcal{G}^{(t)}$  is satisfied. The final iteration count is denoted by  $t^*$ .

At each iteration  $t$ ,  $\boldsymbol{\beta}_{t-1}$  is obtained from (12) using the given index set  $\mathcal{G}^{(t-1)}$ . The  $t$ -th grid index set  $\mathcal{G}^{(t)}$  is then updated by (30) according to the results of  $\boldsymbol{\beta}_{t-1}$  in an iterative manner until convergence. Upon satisfying the termination criterion, the final estimate within the on-grid perspective is defined as

$$\hat{\mathcal{G}} = \arg \min_{\mathcal{G}^{(t-1)}, \mathcal{G}^{(t)}} \{\boldsymbol{\varepsilon}(\boldsymbol{\theta}_{\mathcal{G}^{(t-1)}}), \boldsymbol{\varepsilon}(\boldsymbol{\theta}_{\mathcal{G}^{(t)}})\}. \quad (32)$$

Nevertheless, incoming signals rarely coincide with the predefined grid points. The intervals are defined as

$$\mathcal{R}_i = \left[ \tilde{\theta}_1^i, \tilde{\theta}_2^i \right], \quad (33)$$

where

$$\tilde{\theta}_1^i = \min\{\theta_{g_i^{(t-1)}}, \theta_{g_i^{(t)}}\}, \quad (34)$$

$$\tilde{\theta}_2^i = \max\{\theta_{g_i^{(t-1)}}, \theta_{g_i^{(t)}}\}. \quad (35)$$

Then, the set of ROIs is denoted by

$$\mathcal{R} = \{\mathcal{R}_1, \mathcal{R}_2, \dots, \mathcal{R}_{|\mathcal{G}^{(t)}|}\}. \quad (36)$$

$\mathcal{R}$  can be regarded as the output of the current stage.

If  $\boldsymbol{\varepsilon}(\boldsymbol{\theta}_{\hat{\mathcal{G}}}) < \epsilon$ , a bisection search is employed herein to obtain the final DOA estimates. Analogous to the underlying principle of the iterative process, the ROI intervals are subdivided to evaluate the corresponding spatial angular pseudo-derivative. Subsequently, the ROI boundaries are successively updated to narrow the search range. Once the bisection search concludes, the final estimates  $\hat{\boldsymbol{\theta}}$  are obtained as the summation of the results of bisection method and the corresponding grid bias. If the  $\boldsymbol{\varepsilon}(\boldsymbol{\theta}_{\hat{\mathcal{G}}}) > \epsilon$ , we need to use the following greedy patch mechanism to correct the initialization  ${}^0\mathcal{G}$ .

**Greedy Patch Mechanism:** If the greedy patch mechanism is invoked, it is assumed that the cardinality of  $|\mathcal{G}^{(0)}|$  is less than  $K$ . Accordingly, an additional examination of the spatial spectrum is required to identify the missing signal components. In this paper, we refer to the region between two adjacent spectral peaks as the spectral valley. Subsequently, the high-priority candidate region (HPCR) is denoted by

$$\mathcal{H}^1 = \{\mathcal{H}_1^1, \mathcal{H}_2^1, \dots, \mathcal{H}_{|\Lambda|}^1\}, \quad (37)$$

where

$$\mathcal{H}_i^1 = [\theta_l^i, \theta_r^i], \quad i \in \Lambda, \quad |\Lambda| = |\mathcal{P}| - 1, \quad (38)$$

and  $(\theta_l^i, \theta_r^i)$  is a coupled pair of points which is given by

$$(\theta_l^i, \theta_r^i) = \begin{cases} \theta_l^i = \bar{\theta}_i, \theta_r^i = \bar{\theta}_{i+1}, & |\mathcal{I}_i| = 1, |\mathcal{I}_{i+1}| = 1, \\ \theta_l^i = \bar{\theta}_i, \theta_r^i = \bar{\theta}_{\mathcal{I}_{i+1}}, & |\mathcal{I}_i| = 1, |\mathcal{I}_{i+1}| = 2, \\ \theta_l^i = \bar{\theta}_{\mathcal{I}_i}^2, \theta_r^i = \bar{\theta}_{\mathcal{I}_{i+1}}^1, & |\mathcal{I}_i| = 2, |\mathcal{I}_{i+1}| = 1, \\ \theta_l^i = \bar{\theta}_{\mathcal{I}_i}^2, \theta_r^i = \bar{\theta}_{i+1}, & |\mathcal{I}_i| = 2, |\mathcal{I}_{i+1}| = 2. \end{cases} \quad (39)$$

The low-priority candidate region (LPCR) which represents the beam region is formulated as

$$\mathcal{H}^2 = \left\{ \mathcal{H}_1^2, \mathcal{H}_2^2, \dots, \mathcal{H}_{|\mathcal{P}|}^2 \right\}, \quad (40)$$

where  $\mathcal{H}_i^2 = \mathcal{B}_i$ . We define a function to calculate the average power of the given region, which is given by

$$P_e(\mathcal{H}) = \frac{1}{|\mathcal{H}|} \sum_{\theta \in \mathcal{H}} P_g(\theta), \quad \mathcal{H} \in \mathcal{H}^1 \cup \mathcal{H}^2. \quad (41)$$

Then, utilizing (41) yields two sets

$$P_H = \left\{ P_{H_i} \mid P_{H_i} = P_e(\mathcal{H}_i^1), i \in \Lambda \right\} \quad (42)$$

$$P_L = \left\{ P_{L_i} \mid P_{L_i} = P_e(\mathcal{H}_i^2), i \in [|\mathcal{P}|] \right\} \quad (43)$$

Notably, the sets  $\mathcal{H}^1$  and  $P_H$  can be empty.

The proposed greedy patch mechanism operates sequentially. In the greedy patch mechanism, we assume that the beam region and the spectral valley contain at most three and one incident signals, respectively. The HPCR is prioritized. If the  $\mathcal{H}^1 = \emptyset$ , the algorithm proceeds directly to the LPCR. For the HPCR, the elements within  $P_H$  are first arranged in descending order to retrieve the corresponding index set  $\mathcal{I}_H$ . The sub-regions  $\mathcal{H}_i^1$  within the HPCR are processed sequentially according to the sorted order.

If  $|\min P_g(\theta_{\mathcal{H}_i^1})|$  is commensurate with the noise floor  $n_f$ , then

$$\mathcal{H}^{1*} = \mathcal{H}^1 - \bigcup_{i \in \bar{\Lambda}} \mathcal{H}_i^1, \quad (44)$$

where

$$\bar{\Lambda} = \left\{ i \mid |\min P_g(\theta_{\mathcal{H}_i^1}) - n_f| < \epsilon_p, i \in \Lambda \right\}, \quad (45)$$

and the parameter  $\epsilon_p$  denotes the threshold employed to determine whether  $|\min P_g(\theta_{\mathcal{H}_i^1})|$  is at the noise floor level. Subsequently, we utilize three other pre-determined power benchmarks  $P_{s_1}$ ,  $P_{s_2}$ , and  $P_{s_3}$  which respectively denote the one, two, and three sources power levels to determine the final processing priority.

Each iteration of the Greedy Patch mechanism serves to complement the initial angular set by identifying previously omitted signal components. If the peak power is commensurate with the highest predefined level  $P_{s_3}$ , then the corresponding beam region  $\mathcal{H}_i^2$  is prioritized. The corresponding initial angular set is augmented as

$$\mathcal{I}_i = \left\{ \theta_{\mathcal{I}_i}^1, \theta_{\mathcal{I}_i}^2 \right\} \cup \left\{ (\theta_{\mathcal{I}_i}^1 + \theta_{\mathcal{I}_i}^2)/2 \right\}. \quad (46)$$

Analogously, if the peak power is commensurate with  $P_{s_2}$ , the corresponding initial angular set is updated to

$$\mathcal{I}_i = \begin{cases} \mathcal{I}_i, & |\mathcal{I}_i| = 2, \\ \left\{ \theta_{\mathcal{I}_i}^1, \theta_{\mathcal{I}_i}^2 \right\}, & |\mathcal{I}_i| = 1, \end{cases} \quad (47)$$

Finally, if the peak power aligns with the  $P_{s_1}$  level, the sub-regions in  $\mathcal{H}_i^{1*}$  is prioritized. The corresponding initial angular set is

$$\mathcal{I}_i^{\mathcal{H}} = \left\{ \frac{\theta_h^{r_i} + \theta_h^{l_{i+1}}}{2} \right\}. \quad (48)$$

Upon completion of the HPCR processing, the algorithm proceeds to address the remaining LPCR. Following each update of the index of initial angular set  $\tilde{\mathcal{G}}^{(0)}$ , the SAPD Search Step is re-executed to verify whether the reconstruction residual falls below the recovery threshold  $\epsilon$ . The steps of the SAPD Scheme are outlined in Algorithm 2.

---

Algorithm 2 SAPD Search Algorithm to solve (18)

---

Input: The observation data  $\mathbf{y} \in \mathbb{C}^M$   
Output: DOA Angles  $\hat{\theta}$

- 1: Initialization via Algorithm 1 and get the initialization set  $\mathcal{G}^{(0)}$ .
- 2: for  $i = 1$  to  $M - 1 - |\mathcal{G}^{(0)}|$  do
- 3:     for  $t = 1$  to  $T$  do
- 4:         Calculate the current SAPD via (8) and (13)
- 5:         Update the search angles  $\theta_{\mathcal{G}^{(t)}}$  by (30).
- 6:         if (31) and  $\mathcal{G}^{(t-2)} = \mathcal{G}^{(t)}$  then
- 7:             Output the ROI  $\mathcal{R}$ .
- 8:         end if
- 9:     end for
- 10:    if  $\epsilon(\hat{\theta}) < \epsilon$  then
- 11:         Update ROI by bisection method
- 12:         Get the final DOA estimation  $\hat{\theta}$
- 13:    else
- 14:         Use Greedy Patch mechanism to update the initialization  ${}^0\tilde{\mathcal{G}}$ .
- 15:         Repeat the step 3-9
- 16:    end if
- 17: end for
- 18: return The estimated DOAs  $\hat{\theta}$ .

---

### C. Computational complexity analysis

This subsection evaluates the computational complexity of the proposed SAPD algorithm. Based on the procedure outlined in Algorithm 2, Bartlett beamforming requires  $O(MG)$  operations. The peak-finding function contributes a negligible complexity of  $O(\log G)$ . Consequently, the total cost for the initialization stage is  $C_{\text{init}} = O(MG)$ . In straightforward DOA scenarios where the greedy patch mechanism is bypassed, the total computational complexity depends solely on the numerical cost associated with (8) and (12), and is expressed as

$$C_{\text{SAPD}} = O(MG + 2(t^* + b)(MK^2 + K^3)), \quad (49)$$

where  $b$  is the bisection steps. When  $K \ll M \ll G$ , the complexity of the proposed algorithm reduces to  $C_{\text{SAPD}} \approx O(MG)$ . Such conditions are frequently satisfied in modern array signal processing systems. Consequently, SAPD can achieve the super-resolution accuracy characteristic of sparse reconstruction while maintaining a

computational footprint commensurate with conventional grid-based search methods.

In complex DOA estimation scenarios where the greedy patch mechanism is necessitated, the given initial index set cardinality during the  $i$ -th search cycle is given by  $|\mathcal{G}| = D_i$ . With  $t_i^*$  iterations required per search cycle, the total complexity across  $r$  cycles is formulated as

$$C_{\text{SAPD}} = O(MG + \sum_{i=1}^{r-1} (2t^*(MD_i^2 + D_i^3)) + 2(t^* + b)(MD_r^2 + D_r^3)). \quad (50)$$

Notably, traditional sparse recovery methods, such as SBL, ANM or ISTA-based  $\ell_1$ -norm solvers, entail an  $O(G^3)$  computational burden per iteration. This per-iteration overhead frequently exceeds the total complexity of the proposed SAPD algorithm. Therefore, the proposed algorithm exhibits low computational complexity.

#### D. Convergence Analysis of SAPD Search

In this section, we provide a formal convergence analysis for the proposed SAPD algorithm. Given that the optimization problem formulated in (18) is inherently non-convex, establishing global convergence is generally intractable. Consequently, our analysis focuses on the local convergence properties of the iterative sequence. We first establish the existence of local minima for the constituent subproblems.

**Theorem 1 (Existence of Local Minimizers):** For any given  $|\mathcal{G}| = k$ , any local minimum of the corresponding subproblem in the problem  $(P_D)$  is  $k$ -sparse.

Proof: See Appendix A.  $\blacksquare$

Theorem 1 indicates that, given a specified support size, the landscape of problem  $(P_D)$  is analogous to that of the trimmed Lasso, possessing a multitude of  $k$ -sparse local minima. Subsequently, we demonstrate that both the objective function and the sequence of iterates, subject to the defined constraints, converge to a stationary point.

**Theorem 2 (Monotonicity Convergence):** Let  $\{\boldsymbol{\theta}^t\}$  be the sequence of iterates generated by the SAPD search algorithm. Suppose that the sequence converges to a local minimizer  $\boldsymbol{\theta}^*$ , such that  $\lim_{t \rightarrow \infty} \boldsymbol{\theta}^t = \boldsymbol{\theta}^*$ . If the sequence satisfies the strict contraction property  $\|\boldsymbol{\theta}^t - \boldsymbol{\theta}^*\|_2 < \|\boldsymbol{\theta}^{t-1} - \boldsymbol{\theta}^*\|_2$  whenever the iterates  $\boldsymbol{\theta}^t$  and  $\boldsymbol{\theta}^{t-1}$  lie within the local region of convexity of  $\boldsymbol{\theta}^*$ , then the sequence of objective function values  $\varepsilon(\boldsymbol{\theta}^t)$  and the sequence of spatial angular pseudo-derivative values  $\boldsymbol{\beta}(\boldsymbol{\theta}^t)$  are monotonically non-increasing.

Proof: See Appendix B.  $\blacksquare$

Theorem 2 elucidates the non-divergent behavior of the algorithm as it approaches the stationary point, ensuring robust convergence to a local minimizer. Given that DOA estimation is characterized by rich physical structure rather than being a generic high-dimensional optimization task, we leverage the spatial spectrum for physics-aware initialization. This strategy effectively steers the iterative process away from spurious local minima, thereby enabling the proposed algorithm to consistently attain the global optimum for DOA estimation.

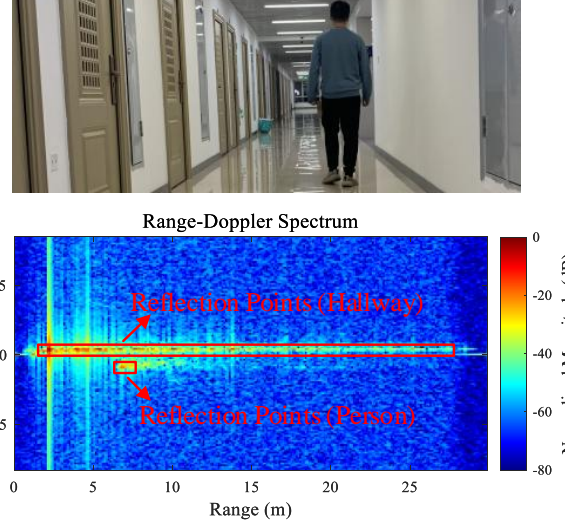


Fig. 3: Reflection Points from the hallway environment and person

#### IV. Numerical Simulations and Experimental Validation

In this section, we conduct numerical simulations to evaluate the performance of the proposed SAPD algorithm. All experiments are performed on a PC equipped with a 2.6 GHz Intel Core i7 processor and 16 GB of RAM. We consider an automotive FMCW radar system equipped with a uniform linear array (ULA) of  $M = 8$  receive antennas. The spacing between adjacent elements is set to  $d_r = \lambda_r/2$ . The Rayleigh resolution limit for this configuration is approximately  $14^\circ$ . The angular domain  $\boldsymbol{\theta} = [-60^\circ, 60^\circ]$  is discretized into a uniform grid with an interval of  $\Delta\theta = 1^\circ$  for the SAPD algorithm. To quantify the estimation accuracy, the root-mean-square error (RMSE) is adopted as the primary performance metric. We define the RMSE as follows

$$\text{RMSE} = \sqrt{\frac{1}{M_t K} \sum_{i=1}^{M_t} \|\hat{\boldsymbol{\theta}}^{(i)} - \boldsymbol{\theta}^*\|_2^2}, \quad (51)$$

where  $\boldsymbol{\theta}^{(i)}$  represents the estimate obtained in the  $i$ -th Monte Carlo trial, and  $M_t$  is the total number of trials. In the following experiments, each RMSE value is computed over  $M_t = 1000$  independent trials.

Regarding the selection of benchmark algorithms, we consider both estimation accuracy and computational efficiency as critical performance metrics. Consequently, computationally intensive methods that exceed a 500-ms processing window, such as StructCovMLE [36], are precluded from our comparison. Furthermore, as this study focuses exclusively on single-snapshot scenarios, subspace-based algorithms [39] that necessitate multiple snapshots for covariance estimation are also omitted. Meanwhile, our study focuses on the sparse DOA estimation method. Thus, the proposed SAPD algorithm is benchmarked against DML [1], IAA-APES [40], OMP [14], ANM [14], VALSE [30], and GSM [26]. For the on-grid method such

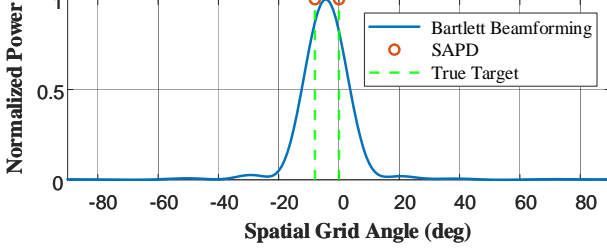


Fig. 4: Normalized spatial spectra for two targets with DOAs of  $0^\circ$  and  $8^\circ$  at SNR = 15dB

as IAA-APES, OMP, and GSM is use the  $\theta = [-60^\circ, 60^\circ]$  with an interval of  $\Delta\theta = 0.5^\circ$ . The signal source  $s(t)$  follows a normal distribution, denoted by  $s(t) \sim \mathcal{N}(30, 1)$ . For algorithms that do not require prior knowledge of the number of sources, such information is withheld during the simulations to evaluate their estimation autonomy.

Example 1 (Real-Time Feasibility and Computational Throughput Evaluation): We first evaluate the real-time feasibility of the proposed algorithm by analyzing its computational throughput. Fig. 3 illustrates a representative Range-Doppler spectrum captured by a TI AWR1843 mmWave radar in a hallway environment with a moving person. It is evident from the RD map that the number of targets to be processed is substantial; following CFAR detection, there are typically 40 to 50 target-occupied RD-cells. Consequently, the DOA estimation must be completed for all such cells within the stringent 50-ms frame interval.

To reflect this workload, we configure a simulation scenario where each RD-cell contains two incident sources. The SNR is set to 15dB. For super-resolution analysis, the incident angles of the two sources are set to  $\theta_1^* = 0^\circ$  and  $\theta_2^*$ , which is varied such that  $\theta_2^* \in \{6, 7, 8\}$ . A representative estimation result of the proposed SAPD search is shown in Fig.4.

In Fig.5((a)), we evaluate the computational throughput by varying the number of detected RD-cells from 1 to 50. The algorithms are executed sequentially, and the total processing latency for successful DOA estimation is recorded. Although OMP exhibits shorter execution times, it is excluded from this comparison due to its insufficient estimation precision, which fails to provide meaningful super-resolution results. The RMSE of OMP represents in the Table I.

As illustrated in Fig.5((a)), for a single RD-cell, the proposed SAPD algorithm is the only method capable of providing valid estimates in under 1 ms. While IAA-APES and VALSE also satisfy the 50-ms frame interval constraint, the remaining benchmarks exceed this threshold. When the workload increases to 10 RD-cells, SAPD remains the sole algorithm operating within the real-time budget, requiring less than 10 ms. For the most demanding case of 50 RD-cells, SAPD completes the estimation in 36.4 ms, effectively maintaining real-time feasibility within the 50-ms window, whereas all other compared

methods require 1000 ms or more. The RMSE performance of the algorithms capable of completing a single RD-cell estimation within 50 ms, namely OMP, IAA-APES, VALSE, and the proposed SAPD, is summarized in Table I. Among these compared algorithms, the proposed SAPD search scheme achieves the minimum RMSE.

TABLE I: The RMSE of four algorithm in the scenario

Methods	OMP	VALSE	IAA-APES	SAPD search
RMSE	4.8988°	0.2130°	0.3453°	<b>0.2035°</b>

Fig. 5((b)) illustrates the superior computational throughput of the proposed algorithm relative to the benchmarks, quantified by the point cloud completion rate CR, which is defined as

$$CR = \frac{N_e}{N_{RD}} \times 100\%, \quad (52)$$

where  $N_e$  denotes the number of successfully processed RD-cells and  $N_{RD}$  represents the total number of detected RD-cells. With the workload set to 40 RD-cells, it is observed that at the 30-ms mark, only our algorithm successfully completes the point cloud generation, thereby providing a 20-ms temporal margin for subsequent radar post-processing tasks. In contrast, even at 40 ms, among the benchmark methods, only IAA-APES and VALSE manage to resolve 2–3 RD-cells. These results from the first set of experiments collectively demonstrate the practical viability of the proposed framework for real-time deployment.

Example 2 (RMSE Performance versus SNR): In this example, we assess the RMSE performance of the proposed algorithm across a range of SNR levels (-5 dB to 25 dB) with  $K = 2$  and an angular separation of  $8^\circ$ .

In Fig.6((a)), to ensure a fair comparison with on-grid algorithms such as DML, GSM, and IAA-APES, the incident angles are set to  $0^\circ$  and  $8^\circ$  to align with the spatial grid. Under this configuration, the SAPD algorithm also operates under the on-grid assumption. The results show that for  $\text{SNR} \geq 15$  dB, SAPD, GSM, and DML asymptotically approach the Cramér-Rao Lower Bound (CRLB) due to the validity of the on-grid assumption. At  $\text{SNR} = 10$  dB, although DML yields the most accurate estimates, its RMSE is only  $0.1^\circ$  lower than those of SAPD, GSM, and VALSE. For  $\text{SNR} < 10$  dB, the proposed algorithm maintains accuracy comparable to DML, GSM, ANM, and VALSE.

Fig.6((b)) evaluates the performance in off-grid scenarios, where a random bias is introduced near  $0^\circ$  while maintaining the  $8^\circ$  separation. For GSM, the off-grid bias is estimated using (12) following the on-grid search, whereas DML and IAA-APES remain uncompensated. The results illustrate that the SAPD accuracy curve nearly overlaps with that of GSM, while DML exhibits a slight performance degradation in this off-grid setting. For  $\text{SNR} \leq 15$  dB, the proposed algorithm achieves precision similar to GSM, DML, VALSE, and ANM. However, for  $\text{SNR} > 15$  dB, gridless methods (VALSE and ANM) provide superior

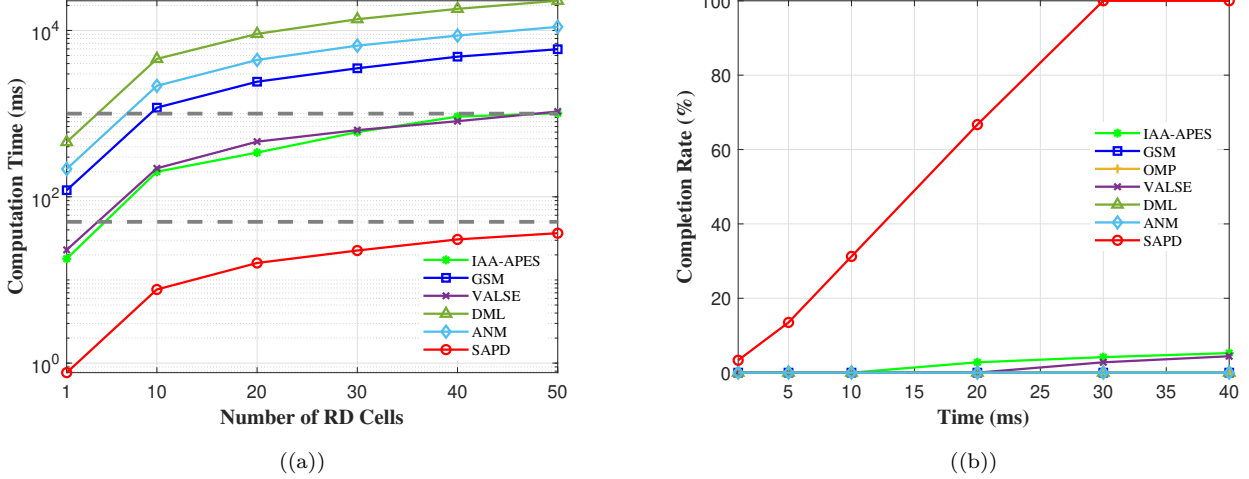


Fig. 5: Computational throughput and real-time feasibility analysis. (a) Total processing latency versus the number of detected RD-cells. (b) Point cloud completion rate versus processing time for  $N_{RD} = 40$ .

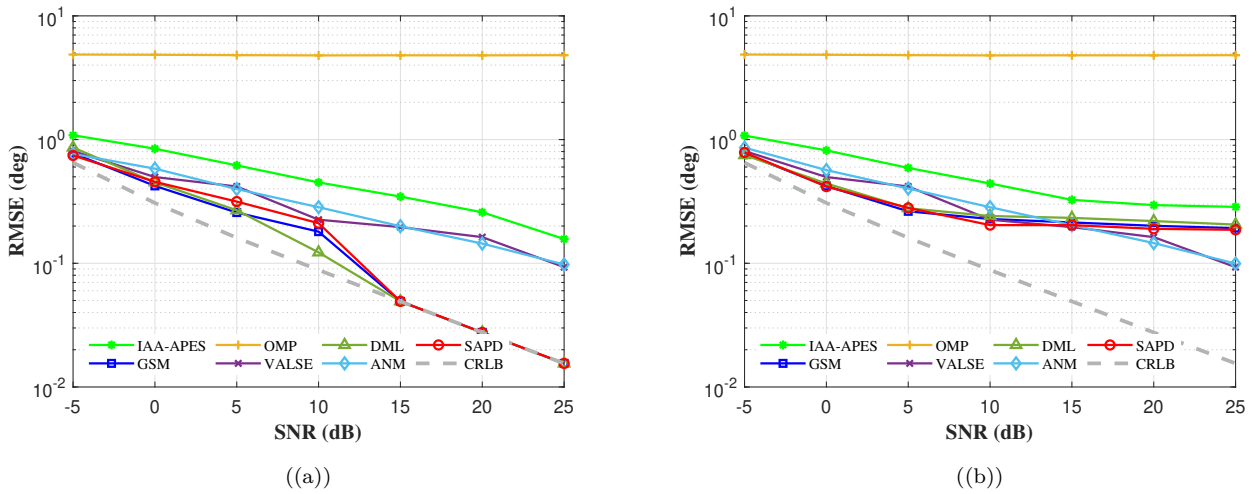


Fig. 6: RMSE performance comparison versus SNR for two incident sources ( $K = 2$ ,  $\Delta\theta = 8^\circ$ ). (a) On-grid scenario ( $0^\circ, 8^\circ$ ). (b) Off-grid scenario with random angular bias.

results. This performance gap is primarily attributed to the approximation error inherent in the first-order Taylor expansion used in the proposed bias estimation.

In summary, as shown in Fig.6((a)) and Fig.6((b)), the estimation accuracy of the proposed SAPD algorithm is on par with high-complexity solvers such as GSM and DML. From a real-time perspective, the proposed method outperforms IAA-APES and matches the precision of VALSE at high SNR levels. Furthermore, while OMP is computationally faster, it fails to resolve the sources in these challenging super-resolution scenarios. Thus, the proposed algorithm provides a superior trade-off between high estimation accuracy and low computational complexity.

**Example 3 (Angular Resolution Performance):** In this example, we investigate the angular resolution capability

of the proposed algorithm. The SNR is maintained at a constant 15dB. We consider two incident sources where the first ground-truth DOA is fixed at  $\theta_1^* = 0^\circ$ , and the angular separation  $\Delta\theta$  is varied from  $2^\circ$  to  $16^\circ$ , such that  $\theta_2^* = \theta_1^* + \Delta\theta$ . Throughout this experiment, an on-grid signal model is adopted to evaluate the resolution limits. Due to the resolution failure of several benchmark algorithms between  $2^\circ$  and  $6^\circ$ , the performance is characterized using two complementary metrics. Fig.7((a)) illustrates the successful rate for angular separations  $\Delta\theta \in [2^\circ, 9^\circ]$ . For larger separations where targets are consistently resolved, Fig. 7((b)) depicts the RMSE performance for  $\Delta\theta \in [8^\circ, 16^\circ]$ .

In Fig.7((a)), the effective estimation is defined as when the estimated source cardinality equals the actual number of incident signals and the precision satisfies

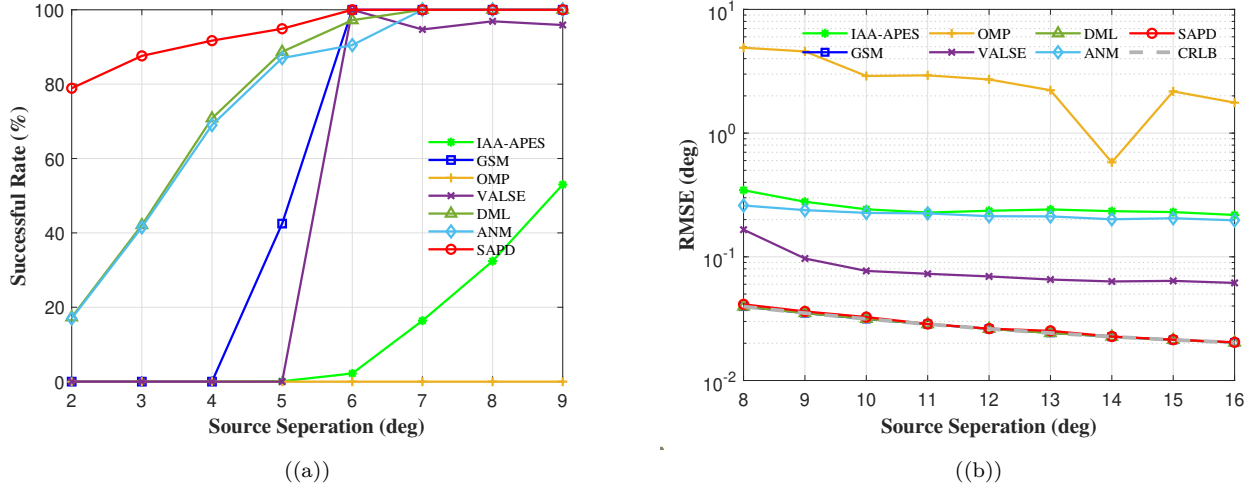


Fig. 7: Performance evaluation versus angular separation  $\Delta\theta$  with SNR = 15dB and  $K = 2$ . (a) Successful rate for  $\Delta\theta \in [2^\circ, 9^\circ]$ . (b) RMSE performance for  $\Delta\theta \in [8^\circ, 16^\circ]$ .

RMSE  $< 0.5^\circ$ . The successful rate represents the percentage of such effective estimates across 1000 trials. As clearly demonstrated in Fig.7((a)), the proposed SAPD algorithm maintains a successful rate of 80% at an angular separation of only  $2^\circ$ , whereas benchmarks such as DML and ANM yield success rates below 20%. Within the range  $\Delta\theta \in [3^\circ, 5^\circ]$ , the success rate of SAPD increases and consistently outperforms all other compared methods. At a  $6^\circ$  separation, both SAPD and GSM achieve full resolution, while DML and ANM only reach this level at  $7^\circ$ . Notably, VALSE exhibits slight performance degradation between  $6^\circ$  and  $9^\circ$ , and IAA-APES suffers from a significantly lower success rate throughout this interval. Finally, OMP is found to be entirely incapable of resolving targets in this super-resolution regime.

As illustrated in Fig.7((b)), under the on-grid assumption, the proposed SAPD algorithm achieves performance parity with DML and GSM, both of which asymptotically approach the CRLB. Synthesizing the results from Fig. 7((a)) and Fig.7((b)), it is evident that our method exhibits remarkable angular resolution, surpassing even computationally intensive methods such as DML and ANM. Notably, the proposed framework is the sole algorithm capable of completing sparse DOA estimation in the super-resolution scenarios within 1ms.

**Example 4 (Parametric Analysis of Computational Efficiency):** In this example, we characterize the relationship between the processing latency of the proposed algorithm and key simulation parameters, including the SNR, angular separation, and the number of sources. This analysis aims to evaluate the sensitivity of the algorithm's computational efficiency to parametric variations. Since OMP fails to provide valid DOA estimates in the considered regimes, its execution time is excluded from Fig. 8 to ensure a meaningful performance comparison.

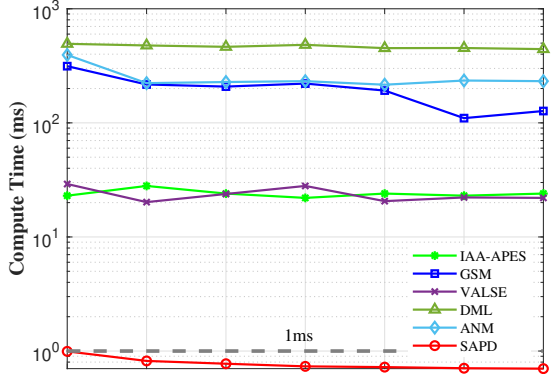
Fig.8((a)) illustrates the relationship between the com-

putational latency of the proposed algorithm and the SNR. Adopting the configuration from Example 2, we evaluate the execution time across the specified SNR range. The results show that the processing time of the SAPD algorithm decreases as the SNR increases, reflecting faster convergence at higher signal qualities. Notably, even at a low SNR of -5dB, the proposed method consistently completes effective DOA estimation within 1ms.

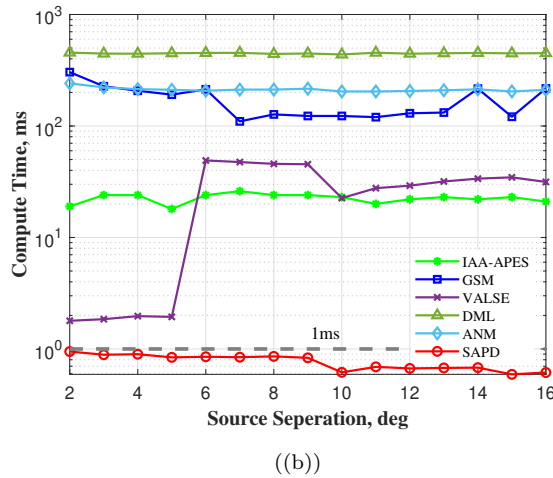
Fig.8((b)) characterizes the computational latency of the proposed algorithm as a function of the angular separation. Following the experimental setup of Example 3, we evaluate the execution time across varying separation distances. It is observed that the processing time of the SAPD algorithm exhibits a marginal reduction as the angular separation increases, suggesting that wider target intervals facilitate slightly faster convergence while maintaining an overall low computational footprint.

Fig.8((c)) illustrates the relationship between processing latency and the number of sources  $K \in \{2, \dots, 7\}$ . To isolate the impact of source cardinality, we maintain an angular separation of at least  $15^\circ$  between targets. The assumption ensures reliable DOA estimation for all benchmark algorithms. Then, the incident angles are generated randomly. A representative estimation result for the seven sources scenario is depicted in Fig. 9. The execution time of the proposed SAPD algorithm exhibits an upward trend as the number of sources increases from 5 to 7. This experimental finding corroborates the theoretical complexity analysis provided in (49).

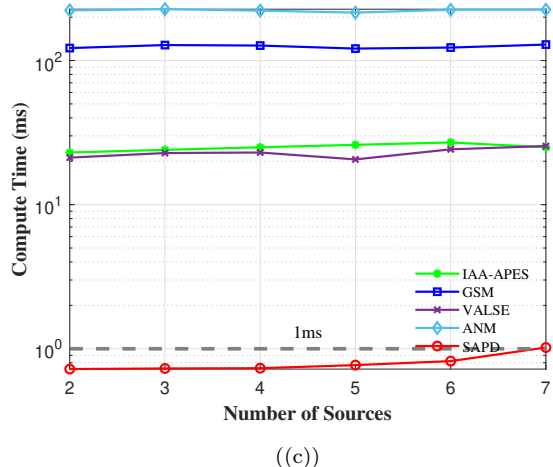
Synthesizing the results across Fig.8, it is evident that the proposed algorithm consistently achieves effective DOA estimation with a latency of less than 1ms, regardless of variations in SNR, angular separation, or the number of sources. These findings validate the computational robustness of the SAPD search under diverse sensing conditions. Consequently, the proposed method satisfies



((a))



((b))



((c))

Fig. 8: Computational time analysis of the proposed SAPD algorithm across various simulation parameters. (a) Processing time versus SNR. (b) Processing time versus angular separation  $\Delta\theta$ . (c) Processing time versus the number of sources  $K$ .

the stringent real-time requirements essential for high-performance automotive radar systems.

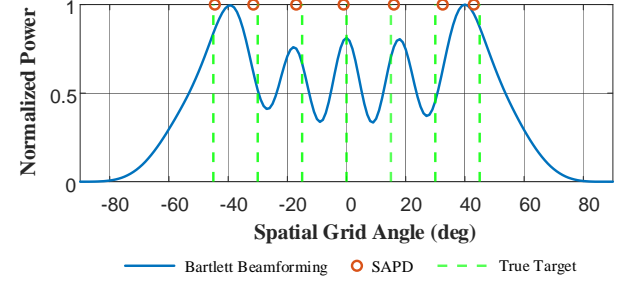


Fig. 9: Normalized spatial spectra for seven targets with DOAs of  $\{-45^\circ, 30^\circ, -15^\circ, 0^\circ, 15^\circ, 30^\circ, 45^\circ\}$  at SNR = 15dB

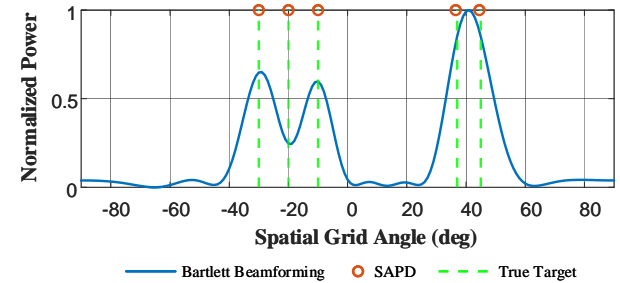


Fig. 10: Normalized spatial spectra for five targets with DOAs of  $\{-30^\circ, -20^\circ, -10^\circ, 37^\circ, 45^\circ\}$  at SNR = 15dB

Example 5 (Effective of Greedy Patch Mechanism): The incident angles are set to  $\theta^* = \{-30^\circ, -20^\circ, -10^\circ, 37^\circ, 45^\circ\}$  at an SNR of 15dB. As illustrated in Fig. 10, the source at  $-20^\circ$  is unresolved in the initial spatial spectrum due to the merging effect, manifesting as a prominent spectral valley between adjacent peaks. Consequently, during the initialization phase of the SAPD search, this target is omitted, resulting in an initial support set with a cardinality of four. To remedy this, the Greedy Patch mechanism is invoked to augment the support set, leading to the final estimation results depicted in Fig. 10.

In view of real-time processing constraints, Table II restricts the RMSE comparison to computationally efficient methods, specifically VALSE, IAA-APES, and the proposed SAPD. Under the specified simulation settings, VALSE fails to resolve the targets, yielding invalid estimates. While IAA-APES achieves an RMSE of  $0.8944^\circ$ , the proposed SAPD algorithm demonstrates superior precision with a significantly lower RMSE of  $0.2724^\circ$ , substantially outperforming the IAA-APES benchmark.

TABLE II: The RMSE of three algorithm in the scenario

Methods	VALSE	IAA-APES	SAPD search
RMSE	—	$0.8944^\circ$	$0.2724^\circ$

Table III summarizes the execution times for the three algorithms. Notably, VALSE incurs a 140ms latency even in cases of estimation failure, whereas IAA-APES requires 30ms. In stark contrast, the proposed SAPD algorithm

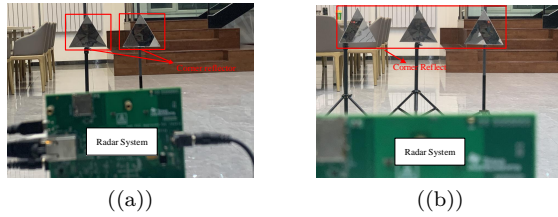


Fig. 11: Experimental scenarios for hardware validation. (a) Two corner reflectors with ground-truth DOAs at  $\Delta\theta \in [-6.5^\circ, 0.5^\circ]$ . (b) Three corner reflectors with ground-truth DOAs at  $\Delta\theta \in [-8.5^\circ, 2^\circ, 12^\circ]$ .

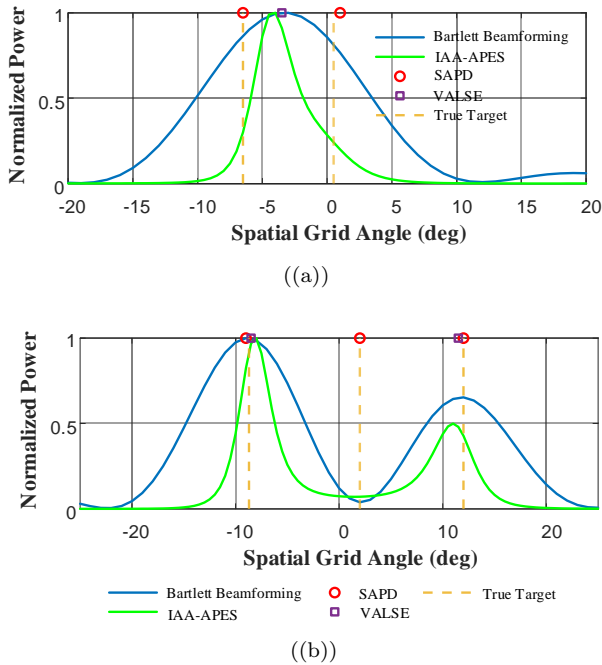


Fig. 12: Normalized experimental spatial spectra for corner reflectors. (a) Two sources at DOAs of  $-6.5^\circ$  and  $0.5^\circ$ . (b) Three sources at DOAs of  $-8.5^\circ$ ,  $2^\circ$  and  $12^\circ$ .

achieves a processing time of merely 1.242 ms, inclusive of the Greedy Patch mechanism overhead.

Consequently, in our opinion, these results further validate that our framework satisfies the stringent requirements of high precision and real-time feasibility, even in complex multi-target scenarios.

TABLE III: The computational time of three algorithm in the scenario

Methods	VALSE	IAA-APES	SAPD search
Computation Time	140ms	30ms	<b>1.242ms</b>

Example 6 (Experimental Validation with Real-World Data): In this example, we validate the performance of the proposed algorithm using raw radar data captured by a TI AWR1843 mmWave radar system. Corner reflectors are employed as targets and are positioned within the same RD-cell to create a challenging super-resolution scenario,

as illustrated in Fig. 11. In the first case (Fig. 11((a))), two corner reflectors are placed at  $\{-6.5^\circ, 0.5^\circ\}$ . In the second case (Fig. 11((b))), three reflectors are arranged at  $\{-8.5^\circ, 2^\circ, 12^\circ\}$ . The estimation results for IAA-APES, VALSE, and the proposed SAPD algorithm are compared in Fig. 12. It is evident that in both scenarios, only our proposed SAPD algorithm successfully identifies the correct number of sources while providing high-precision DOA estimates, whereas the benchmark methods fail to resolve the closely spaced targets.

## V. Conclusion

This paper introduced the spatial angular pseudo-derivative framework, a sparse DOA estimation scheme specifically designed for single-snapshot, high-precision, and real-time applications under stringent computational constraints. By leveraging the concept of the spatial angular pseudo-derivative, we transformed the high-dimensional sparse recovery task into an efficient search-based solver. Theoretical analysis demonstrates that the proposed algorithm has low computational complexity, and numerical results indicate that the proposed scheme achieves millisecond execution times without compromising estimation fidelity. Notably, its resolution capability exceeds that of several high-complexity methods like DML. The practical effectiveness of the SAPD algorithm was further verified using raw radar data collected from a hardware platform. Given its superior performance and minimal computational footprint, the SAPD algorithm represents a promising solution for the sensing requirements of next-generation autonomous driving.

## Appendix A Proof of Theorem 1

The optimization problem ( $P_D$ ) can be reformulated as the minimization of the penalized objective:

$$\mathbf{x} = \arg \min_{\mathbf{x}} \frac{1}{2} \|\mathbf{y} - \mathbf{A}(\boldsymbol{\theta})\mathbf{x}(\boldsymbol{\theta})\|_2^2 + \lambda \tau_k(\mathbf{x}(\boldsymbol{\theta})) \quad (53)$$

where  $\tau_k(\mathbf{x}(\boldsymbol{\theta})) = \sum_{i=k+1}^N |\mathbf{x}|_{(i)}$  is the trimmed lasso of the ordered components  $|\mathbf{x}|_{(1)} \geq |\mathbf{x}|_{(2)} \geq \dots \geq |\mathbf{x}|_{(G)}$ .

For a fixed support set  $|\mathcal{G}| = k$ , the subproblem assumes that all components  $\theta_i$  for  $i \notin \mathcal{G}$  are zero, which implies  $\tau(\boldsymbol{\theta}) = 0$ . By choosing a penalty parameter  $\lambda$  such that

$$\lambda \geq \|\mathbf{y}\|_2 \cdot \max_{i=1, \dots, d} \|\mathbf{a}\|_2 \quad (54)$$

the penalty term effectively enforces the cardinality constraint. Consequently, the local minimizers of the penalized objective satisfy the  $k$ -sparse requirement. ■

## Appendix B Proof of Theorem 2:

Consider the objective function  $\varepsilon(\boldsymbol{\theta}) = \|\mathbf{y} - \mathbf{A}(\boldsymbol{\theta})\mathbf{x}(\boldsymbol{\theta})\|_2$ . To establish the convergence, we identify a corresponding Lyapunov-like potential function  $J(\boldsymbol{\theta})$ , defined as the squared orthogonal projection residual

$$J(\boldsymbol{\theta}) = \|\mathbf{I} - \mathbf{P}_{\mathbf{A}}(\boldsymbol{\theta})\mathbf{y}\|_2^2 = \varepsilon^2(\boldsymbol{\theta}) \quad (55)$$

where  $P_A(\theta) = \mathbf{A}(\mathbf{A}^H \mathbf{A})^{-1} \mathbf{A}^H$  denotes the orthogonal projection matrix onto the column space of  $\mathbf{A}(\theta)$ .

To establish the monotonic descent property of the sequence  $\varepsilon(\theta^t)$ , it is sufficient to analyze the convergence behavior of the Lyapunov candidate function  $J(\theta)$ . Since  $\theta^*$  is a local minimizer of the smooth concentrated cost function  $J(\theta)$ , it satisfies the first-order optimality condition, which  $\nabla J(\theta^*) = 0$ . Within the local region of convexity surrounding  $\theta^*$ , we apply a second-order Taylor expansion of  $J(\theta)$  at the  $t$ -th iterate

$$J(\theta^t) \approx J(\theta^*) + \frac{1}{2}(\theta^t - \theta^*)^T \mathbf{H}(\theta^*)(\theta^t - \theta^*), \quad (56)$$

where  $\mathbf{H}(\theta^*)$  denotes the Hessian matrix of  $J(\theta)$  evaluated at  $\theta^*$ . Given that  $\theta^*$  is a strict local minimizer, the Hessian matrix  $\mathbf{H}(\theta^*)$  is positive definite.

Under this condition, the function value  $J(\theta)$  is strictly increasing with respect to the weighted Euclidean distance from  $\theta^*$ . According to the strict contraction property assumed in the theorem, we have  $\|\theta^t - \theta^*\|_2 < \|\theta^{t-1} - \theta^*\|_2$ . In the vicinity of  $\theta^*$  where the landscape is locally convex and the eigenvalues of  $\mathbf{H}(\theta^*)$  are bounded, this parameter-space contraction directly implies a reduction in the quadratic form, yielding

$$J(\theta^t) \leq J(\theta^{t-1}). \quad (57)$$

Since  $\varepsilon(\theta^t) = \sqrt{J(\theta^t)}$ , the monotonicity of the square root function for non-negative arguments ensures that

$$\varepsilon(\theta^t) \leq \varepsilon(\theta^{t-1}). \quad (58)$$

This confirms that the objective function sequence  $\varepsilon(\theta^t)$  is monotonically non-increasing, which completes the proof.  $\blacksquare$

Analogously, the sequence of spatial angular pseudo-derivative values  $\beta(\theta^t)$  is also monotonically non-increasing.

## References

- [1] H. Krim and M. Viberg, "Two decades of array signal processing research: The parametric approach," *IEEE Signal Process Mag.*, vol. 13, no. 4, pp. 67–94, JUL 1996.
- [2] W. Liu, M. Haardt, M. S. Greco, C. F. Mecklenbräuker, and P. Willett, "Twenty-five years of sensor array and multichannel signal processing: A review of progress to date and potential research directions," *IEEE Signal Process Mag.*, vol. 40, no. 4, pp. 80–91, 2023.
- [3] S. Sun and Y. D. Zhang, "4D automotive radar sensing for autonomous vehicles: A sparsity-oriented approach," *IEEE J. Sel. Top. Signal Process.*, vol. 15, no. 4, pp. 879–891, 2021.
- [4] M. Jiang, G. Xu, H. Pei, Z. Feng, S. Ma, H. Zhang, and W. Hong, "4D high-resolution imagery of point clouds for automotive mmwave radar," *IEEE Trans. Intell. Transp. Syst.*, vol. 25, no. 1, pp. 998–1012, 2024.
- [5] A. Venon, Y. Dupuis, P. Vasseur, and P. Merriaux, "Millimeter wave fmcw radars for perception, recognition and localization in automotive applications: A survey," *IEEE Trans. Intell. Veh.*, vol. 7, no. 3, pp. 533–555, 2022.
- [6] Z. Hong, Y. Petillot, and S. Wang, "Radar slam: Radar based large-scale slam in all weathers," in *Proc. IEEE/RSJ Int. Conf. Intell. Robots Syst.*, 2020, pp. 5164–5170.
- [7] Y. Cheng, J. Su, M. Jiang, and Y. Liu, "A novel radar point cloud generation method for robot environment perception," *IEEE Trans. Rob.*, vol. 38, no. 6, pp. 3754–3773, 2022.
- [8] S. Sun, A. P. Petropulu, and H. V. Poor, "MIMO radar for advanced driver-assistance systems and autonomous driving: Advantages and challenges," *IEEE Signal Process Mag.*, vol. 37, no. 4, pp. 98–117, 2020.
- [9] S. G. Casspi, J. Tabrikian, and H. Messer, "Blind array calibration of mutual coupling, phase, and gain for automotive radar," *IEEE Trans. Aerosp. Electron. Syst.*, vol. 60, no. 1, pp. 1060–1073, 2024.
- [10] H. D. Mafukidze, A. K. Mishra, J. Pidanic, and S. W. P. Francois, "Scattering centers to point clouds: A review of mmwave radars for non-radar-engineers," *IEEE Access*, vol. 10, pp. 110992–111021, 2022.
- [11] Y. Wu, C. Li, Y. T. Hou, and W. Lou, "A real-time super-resolution doa estimation algorithm for automotive radar sensor," *IEEE Sensors Journal*, vol. 24, no. 22, pp. 37947–37961, 2024.
- [12] J. Jiang, S. Xu, K. Zhang, J. Wei, J. Wang, and S. Wang, "Digital beamforming enhanced radar odometry," in *Proc. 2025 IEEE Int. Conf. Robot. Automat.*, 2025, pp. 4601–4607.
- [13] W. Rueckner and C. Papaliolios, "How to beat the rayleigh resolution limit: A lecture demonstration," *Amer. J. Phys.*, vol. 70, no. 6, pp. 587–594, May 2002.
- [14] Z. Yang, J. Li, P. Stoica, and L. Xie, "Sparse methods for direction-of-arrival estimation," in *Proc. Acad. Press Library Signal Process.* Elsevier, 2018, pp. 509–581.
- [15] P. Chen, Z. Chen, Z. Cao, and X. Wang, "A new atomic norm for doa estimation with gain-phase errors," *IEEE Trans. Signal Process.*, vol. 68, pp. 4293–4306, 2020.
- [16] M. Esfandiari and S. A. Vorobyov, "Generalized framework to subspace-based doa estimation," *IEEE Trans. Signal Process.*, vol. 73, pp. 3872–3885, 2025.
- [17] G. Itzhak and I. Cohen, "Stft-domain least-distortion region-of-interest beamforming," *IEEE Trans. Audio Speech Lang. Process.*, vol. 33, pp. 2803–2816, 2025.
- [18] B. K. Natarajan, "Sparse approximate solutions to linear systems," *SIAM J. Comput.*, vol. 24, no. 2, pp. 227–234, 1995.
- [19] R. SCHMIDT, "Multiple emitter location and signal parameter estimation," *IEEE Trans. Antennas Propag.*, vol. 34, no. 3, pp. 276–280, MAR 1986.
- [20] R. ROY and T. KAILATH, "Esprit-estimation of signal parameters via rotational invariance techniques," *IEEE Trans. Acoust., Speech, Signal Process.*, vol. 37, no. 7, pp. 984–995, JUL 1989.
- [21] D. Malioutov, M. Cetin, and A. Willsky, "A sparse signal reconstruction perspective for source localization with sensor arrays," *IEEE Trans. Signal Process.*, vol. 53, no. 8, 2, pp. 3010–3022, AUG 2005.
- [22] D. Wipf and S. Nagarajan, "Iterative reweighted  $\ell_1$  and  $\ell_2$  methods for finding sparse solutions," *IEEE J. Sel. Top. Signal Process.*, vol. 4, no. 2, pp. 317–329, 2010.
- [23] Y. Cheng, T. Liu, J. Shi, D. Guan, Z. Liu, Y. Liu, and X. Li, "Generalized gridless formulation of reweighted  $\ell_{2,1}$  minimization for doa estimation," *IEEE Trans. Aerosp. Electron. Syst.*, vol. 61, no. 2, pp. 2295–2308, 2025.
- [24] E. Soubies, L. Blanc-Féraud, and G. Aubert, "A continuous exact  $\ell_0$  penalty (cel0) for least squares regularized problem," *SIAM J. Imag. Sci.*, vol. 8, no. 3, pp. 1607–1639, 2015.
- [25] E. Soubies, A. Chinatto, P. Larzabal, J. M. T. Romano, and L. Blanc-Féraud, "Direction-of-arrival estimation through exact continuous  $\ell_{2,0}$ -norm relaxation," *IEEE Signal Process Lett.*, vol. 28, pp. 16–20, 2021.
- [26] T. Amir, R. Basri, and B. Nadler, "The trimmed lasso:

Sparse recovery guarantees and practical optimization by the generalized soft-min penalty,” *SIAM J. Math. Data Sci.*, vol. 3, no. 3, pp. 900–929, 2021.

[27] A. A. Salama, M. A. Shawky, S. H. Darwish, A. A. Elmahallawy, M. A. Elaziz, A. Almogren, A. G. Abdellatif, and S. T. Shah, “Unlocking the dynamic potential: Next-gen doa estimation for moving signals via bscs with adaptive weighted kalman filter in 6g networks,” *Internet Things*, vol. 30, p. 101486, 2025.

[28] Z. Yang, L. Xie, and C. Zhang, “Off-grid direction of arrival estimation using sparse bayesian inference,” *IEEE Trans. Signal Process.*, vol. 61, no. 1, pp. 38–43, 2013.

[29] Y. Jin, D. He, S. Wei, and W. Yu, “Off-grid doa estimation method based on sparse bayesian learning with clustered structural-aware prior information,” *IEEE Trans. Veh. Technol.*, vol. 73, no. 4, pp. 5469–5483, 2024.

[30] M.-A. Badiu, T. L. Hansen, and B. H. Fleury, “Variational bayesian inference of line spectra,” *IEEE Trans. Signal Process.*, vol. 65, no. 9, pp. 2247–2261, 2017.

[31] J. Yang and Y. Yang, “Sparse bayesian doa estimation using hierarchical synthesis lasso priors for off-grid signals,” *IEEE Trans. Signal Process.*, vol. 68, pp. 872–884, 2020.

[32] D. M. Blei, A. Kucukelbir, and J. D. McAuliffe, “Variational inference: A review for statisticians,” *J. Am. Stat. Assoc.*, vol. 112, no. 518, pp. 859–877, 2017.

[33] G. Tang, B. N. Bhaskar, P. Shah, and B. Recht, “Compressed sensing off the grid,” *IEEE Trans. Inf. Theory*, vol. 59, no. 11, pp. 7465–7490, 2013.

[34] Y. Wu, M. B. Wakin, and P. Gerstoft, “Gridless doa estimation with multiple frequencies,” *IEEE Trans. Signal Process.*, vol. 71, pp. 417–432, 2023.

[35] Q. Wang, Z. Zhao, Z. Chen, and Z. Nie, “Grid evolution method for doa estimation,” *IEEE Trans. Signal Process.*, vol. 66, no. 9, pp. 2374–2383, 2018.

[36] R. R. Pote and B. D. Rao, “Maximum likelihood-based gridless doa estimation using structured covariance matrix recovery and sbl with grid refinement,” *IEEE Trans. Signal Process.*, vol. 71, pp. 802–815, 2023.

[37] P. Stoica, P. Babu, and J. Li, “Spice: A sparse covariance-based estimation method for array processing,” *IEEE Trans. Signal Process.*, vol. 59, no. 2, pp. 629–638, 2011.

[38] Y. Wu, A. Jakobsson, and L. Liu, “Super-resolution direction of arrival estimation using a minimum mean-square error framework,” *Signal Process.*, vol. 212, p. 109164, 2023.

[39] M. Esfandiari and S. A. Vorobyov, “Generalized framework to subspace-based doa estimation,” *IEEE Trans. Signal Process.*, vol. 73, pp. 3872–3885, 2025.

[40] T. Yardibi, J. Li, P. Stoica, M. Xue, and A. B. Baggeroer, “Source localization and sensing: A nonparametric iterative adaptive approach based on weighted least squares,” *IEEE Transactions on Aerospace and Electronic Systems*, vol. 46, no. 1, pp. 425–443, 2010.